Fracture toughness of semi-regular lattices

Milad Omidi, Luc St-Pierre*

Aalto University, Department of Mechanical Engineering, Otakaari 4, 02150 Espoo, Finland.

Abstract

Previous studies have shown that the kagome lattice has a remarkably high fracture toughness. This architecture is one of eight semi-regular tessellations, and this work aims to quantify the toughness of three other unexplored semi-regular lattices: the snub-trihexagonal, snub-square and elongated-triangular lattices. Their mode I fracture toughness was obtained with finite element simulations, using the boundary layer technique. These simulations showed that the fracture toughness K_{Ic} of a snub-trihexagonal lattice scales linearly with relative density $\bar{\rho}$. In contrast, the fracture toughness of snub-square and elongated-triangular lattices scale as $\bar{\rho}^{1.5}$, an exponent different from other prismatic lattices reported in the literature. These numerical results were then compared with fracture toughness tests performed on Compact Tension specimens made from a ductile polymer and produced by additive manufacturing. The numerical and experimental results were in excellent agreement, indicating that our samples had a sufficiently large number of unit cells to measure the asymptotic fracture toughness. This result may be useful to guide the design of future experiments.

Keywords: Semi-regular lattices, Fracture toughness, Finite Element simulation, Fracture test

*Corresponding Author

Email address: luc.st-pierre@aalto.fi (Luc St-Pierre)

1. Introduction

Lattice materials are not only light, stiff and strong, but they also have a high fracture toughness (O'Masta et al., 2017; Gu et al., 2019; Liu et al., 2020). Optimising the architecture of lattice materials to maximise their elastic modulus and strength has been the subject of many investigations, and a few highly efficient designs have now been identified (Berger et al., 2017; Tancogne-Dejean et al., 2018; Hsieh et al., 2019). These designs have properties that are close to the theoretical bounds on elastic modulus and strength, leaving marginal room for further improvements. In contrast, the fracture toughness is unbounded and many architectures have remained unexplored.

The effect of architecture on the fracture toughness has been documented for a few prismatic (2D) lattices. Analytical studies (Ashby, 1983; Gibson and Ashby, 1997; Chen et al., 1998; Lipperman et al., 2007; Quintana-Alonso and Fleck, 2009; Berkache et al., 2022), Finite Element (FE) simulations (Fleck and Qiu, 2007; Quintana-Alonso and Fleck, 2007; Romijn and Fleck, 2007), and experiments (Huang and Gibson, 1991; Quintana-Alonso et al., 2010; Seiler et al., 2019) have shown that the fracture toughness of elastic-brittle lattices can be expressed as:

$$K_{Ic} = D\bar{\rho}^{d}\sigma_{ts}\sqrt{\ell}, \tag{1}$$

where $\bar{\rho}$ is the relative density of the lattice, ℓ is the length of the cell walls, σ_{ts} is the tensile strength of the parent material, and the constants D and d are topology-dependent and listed in Table 1 for five prismatic lattices (which are shown in Fig. 1). This scaling law was later extended to ductile lattices by Tankasala et al. (2015). They assumed that the parent material follows the Ramberg-Osgood relationship, where the strain ϵ and stress σ are related by:

$$\frac{\epsilon}{\epsilon_{0s}} = \frac{\sigma}{\sigma_{0s}} + \left(\frac{\sigma}{\sigma_{0s}}\right)^{n}, \tag{2}$$

where ϵ_{0s} and σ_{0s} are the yield strain and stress, respectively, and n is the strain-hardening exponent. Their simulations showed that the effect of ductility can be captured by adding

Table 1: Constants D and d in Eq. (1) for different prismatic lattices. Data collected from Fleck and Qiu (2007) and Romijn and Fleck (2007).

Topology	D	d
Kagome	0.212	0.5
Triangular	0.500	1
Hexagonal	0.800	2
Square 0/90°	0.278	1
Square ±45°	0.216	1

a term in Eq. (1), which becomes:

$$K_{Ic} = D' \bar{\rho}^d \sigma_{0s} \sqrt{\ell} \left(\frac{\epsilon_f}{\epsilon_{0s}} \right)^{\frac{n+1}{2n}}, \tag{3}$$

where ϵ_f is the failure strain of the parent material. Their results showed that the constant D' can be sensitive to the degree of strain hardening n; therefore, it is not necessarily equal to D in Eq. (1). In contrast, the exponent d was identical for both elastic-brittle and ductile lattices. Even though fracture toughness tests have been conducted on a few ductile lattices (Alsalla et al., 2016; O'Masta et al., 2017; Gu et al., 2018, 2019; Daynes et al., 2021; Li et al., 2021), there are, to the best of our knowledge, no direct comparison between Eq. (3) and experiments.

The results in Table 1 show that the exponent d may take three different values. In general, bending-dominated architectures, such as the hexagonal lattice, have $d = 2$ (Gibson and Ashby, 1997). Otherwise, stretching-dominated topologies, like the triangular lattice or the 3D octet truss, have an exponent $d = 1$ (Fleck and Qiu, 2007; O'Masta et al., 2017). The kagome lattice, however, has an unusual behaviour: despite being stretching-dominated, it has a lower value of d, making it significantly tougher than other architectures at low relative densities. The kagome lattice is also geometrically different from other architectures listed in Table 1. The hexagonal, square, and triangular lattices are classified as regular tessellations, meaning that they are made from a single regular polygon, see Fig. 1. In contrast, the kagome lattice is assembled from two regular polygons and is therefore classified as a semi-regular tessellation (Williams, 1979). There are seven other semi-regular tessellations, see Fig. 1, and this work aims to quantify their fracture toughness.

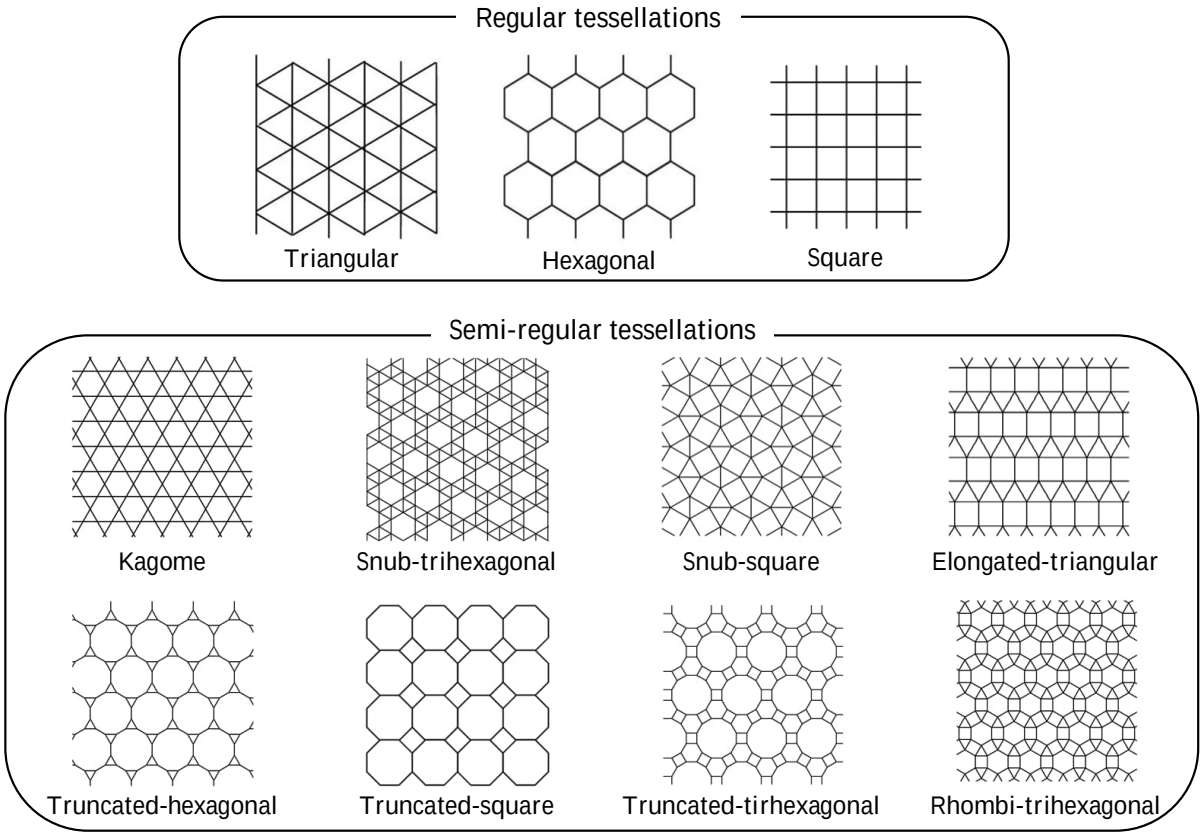

Figure 1: Examples of prismatic lattices: there are three regular and eight semi-regular tessellations. Regular lattices are made from a single regular polygon, whereas semi-regular tessellations are assembled from multiple regular polygons. The nomenclature is based on Williams (1979).

Our study will focus on snub-trihexagonal, snub-square and elongated-triangular lattices (see Fig. 1) as they are the stiffest and strongest semi-regular tessellations (Omidi and St-Pierre, 2022). The other four semi-regular lattices are bending-dominated; therefore, their fracture toughness is expected to be low and comparable to the hexagonal lattice with $d = 2$. We will show that the snub-trihexagonal has a fracture toughness similar to the triangular lattice with $d = 1$, whereas the snub-square and elongated-triangular lattices exhibit a unique behaviour with $d = 1.5$, an exponent different from other prismatic lattices listed in Table 1. Our study includes both FE simulations and experiments: the predictions will be used to calibrate Eq. (3), which will then be compared to fracture toughness tests.

This article is structured as follows. The numerical modelling approach and the testing procedure are described in Section 2. Then, the numerical and experimental results are

presented in Section 3, followed by a discussion in Section 4.

2. Material and methods

2.1. Numerical modelling approach

The fracture toughness of each lattice was predicted using Finite Element (FE) simulations. All simulations were done with the implicit solver of the commercial software Abaqus and assuming finite strain. We used the boundary layer method, which was introduced by Schmidt and Fleck (2001) and then used in many other studies (Fleck and Qiu, 2007; Romijn and Fleck, 2007; Tankasala et al., 2015; Gu et al., 2018), to ensure that our results can be directly compared to those presented in Table 1.

For each tessellation, we used a square domain with a side length of 300ℓ, where ℓ is the length of a cell wall. The domain contained an initial crack in the negative x_1 direction, as shown in Fig. 2a. A detailed view of the position of the initial crack is given in Fig. 2b-d for each architecture. Additional simulations (not included here) showed that moving the crack tip to a different cell had a negligible effect on the fracture toughness. All bars were meshed using Timoshenko beam elements (B21 code in Abaqus); 50 elements per bar were used around the crack tip ($r \leq 30\ell$, see Fig. 2a), whereas 10 elements per bar were used elsewhere. A mesh convergence analysis revealed that further refinements had a negligible effect on the predicted fracture toughness.

Each node on the outer boundary of the domain had an applied displacement based on the K_I asymptotic field, see Fig. 2a. The snub-trihexagonal lattice is isotropic (Omidi and St-Pierre, 2022) and therefore, the displacement field (u_1 and u_2) had the form:

$$u_i = \frac{K_I\sqrt{r}}{G} f_i(\theta), \tag{4}$$

where r and θ are the polar coordinates of each node (see Fig. 2a), the functions $f_i(\theta)$ are given in (Williams, 1952), and G is the shear modulus of the snub-trihexagonal lattice, which is detailed in (Omidi and St-Pierre, 2022). Otherwise, the displacement field for the orthotropic snub-square and elongated-triangular lattices was obtained from (Liu et al., 1998). The orthotropic displacement field is similar to Eq. (4), except that the functions f_i also depend upon the relative density $\bar{\rho}$.

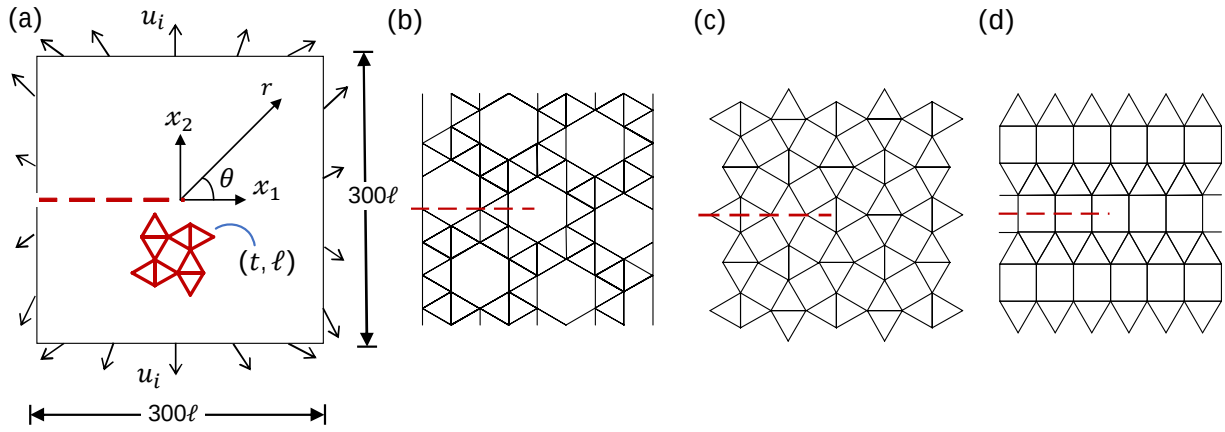

Figure 2: (a) Domain used in the finite element predictions. The dashed red line indicate the position of the initial crack for (b) snub-trihexagonal, (c) snub-square, and (d) elongated-triangular lattices.

In all cases, the cell wall material was assumed to follow the Ramberg-Osgood relationship detailed in Eq. (2). The degree of strain hardening n and the failure strain ϵ_f were varied in the simulations while keeping the yield strain $\epsilon_{0s} = 0.02$ and the yield strength $\sigma_{0s} = 45\,\text{MPa}$ fixed. These values of ϵ_{0s} and σ_{0s} are representative of the polymer used later in the experiments, see Section 2.2. Finally, the fracture toughness K_{Ic} corresponds to the value of K_I when the maximum strain in any element reaches the failure strain ϵ_f.

2.2. Specimen design, manufacturing and testing

Fracture toughness tests were performed to corroborate the numerical simulations. All tests were done on Compact Test (CT) specimens, and their dimensions are given in Fig. 3 for each topology. The width W, and crack length a were slightly different for each lattice, but selected to ensure that $a/W \approx 0.25$, as recommended in ASTM E1820 (2018). All samples had a depth $B = 15\,\text{mm}$ in the prismatic direction. For each architecture, three values of relative density were produced, $\bar{\rho} = 0.2$, 0.25, and 0.3. This was done by keeping the bar length fixed to $\ell = 6\,\text{mm}$, and changing the cell wall thickness t (the relationship between $\bar{\rho}$ and t/ℓ is given in Omidi and St-Pierre (2022) for each topology). Note that additional FE simulations were conducted to ensure that the CT samples had a sufficiently large number of unit cells to provide an accurate measurement of the fracture toughness. This analysis is detailed in Appendix A.

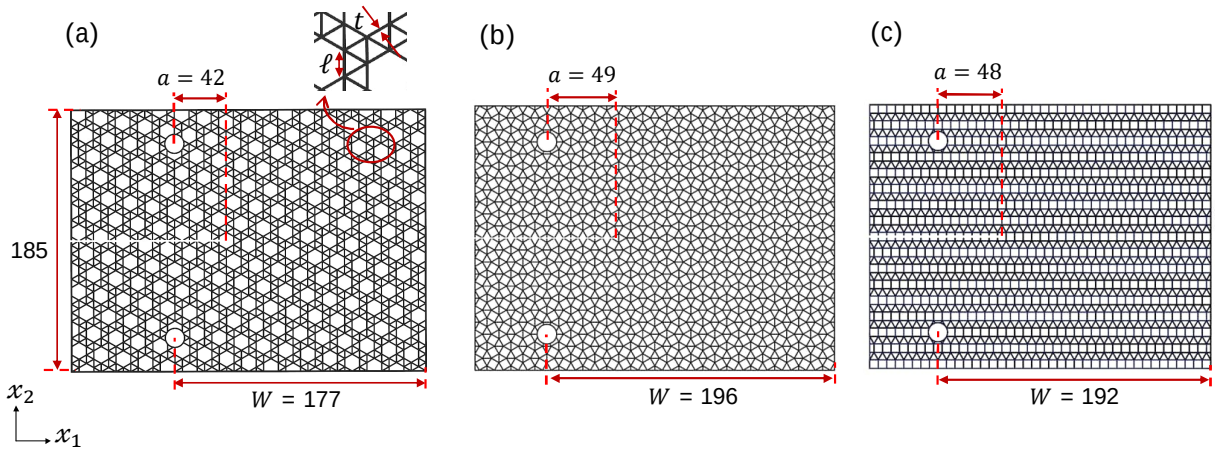

Figure 3: Dimensions of compact tension specimens for (a) snub-trihexagonal, (b) snub-square, and (c) elongated-triangular lattices. All dimensions are in mm. Samples had a depth $B = 15\,\text{mm}$ in the prismatic direction.

All samples were manufactured by additive manufacturing; more specifically, by stereolithography using a Form 3L machine from Formlabs. First, the geometry was created in Abaqus and a stl file was exported to the Form 3L machine. Second, the specimen was printed with a layer thickness of $50\,\mu\text{m}$ and using the Formlabs Clear resin. All samples were printed with their prismatic axis perpendicular to the printing bed. After printing, the lattice was washed in an isopropyl alcohol (IPA) solution and post-cured under UV light at a temperature of 60° C for 30 min, as recommended in the Formlabs documentation.

All CT samples were tested using a MTS electromechanical testing machine with a capacity of 30 kN and with a constant displacement rate of 2 mm/min. Both the force and load-line displacement were recorded by the testing machine. For each test, the fracture toughness was calculated according to (ASTM E1820, 2018):

$$K_{Ic} = \frac{P_{max}}{B\sqrt{W}}\, f\left(\frac{a}{W}\right), \tag{5}$$

where P_{max} is the maximum force; the dimensions B, W and a are given in Fig. 3; and the function $f(a/W)$ is given in ASTM E1820 (2018). We emphasise that Eq. (5) is based on linear elastic fracture mechanics, but this assumption is supported by the measured responses, which are presented in Section 3.2.

Tensile tests were conducted to measure the response of the Clear resin used to manu-

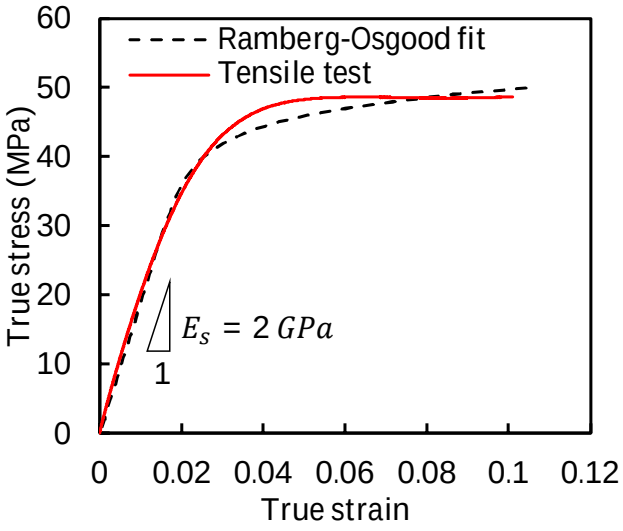

Figure 4: Measured tensile response of the Clear resin used to manufacture all samples. The response is accurately modelled by the Ramberg-Osgood relationship, Eq. (2), with $\sigma_{0s} = 45\,\text{MPa}$, $\epsilon_{0s} = 0.02$, and $n = 13$.

facture all CT samples. Following the procedure detailed above, dog-bone specimens were fabricated with dimensions comparable to those of the cell walls in the CT samples. The tensile specimens had a gauge length of 10 mm, a width of 10 mm, and a thickness of 0.50 mm. Ten tests were conducted at a strain-rate of $5 \cdot 10^{-4}\,\text{s}^{-1}$ and the average material properties were: a Young's modulus $E_s = 2.0 \pm 0.10\,\text{GPa}$, a yield strength $\sigma_{0s} = 45 \pm 3\,\text{MPa}$, and a failure strain $\epsilon_f = 0.10 \pm 0.02$. A measured stress-strain curve is given in Fig. 4 for a sample with properties close these average values.

3. Results

3.1. Numerical results

The fracture toughness of each lattice, predicted with FE simulations, is plotted as a function of relative density in Fig. 5 and 6. Results are shown for different values of failure strain ϵ_f in Fig. 5, while keeping the degree of strain hardening fixed at $n = 13$. In contrast, Fig. 6 shows the effect of the strain hardening exponent n, for a fixed value $\epsilon_f = 0.1$. In both figures, the relative density $\bar{\rho} \geq 0.1$ to ensure that buckling does not occur before fracture (Shaikeea et al., 2022). In all cases, the first cell wall to fracture is the vertical bar in front of the crack tip, as shown on the deformed meshes in Fig. 7.

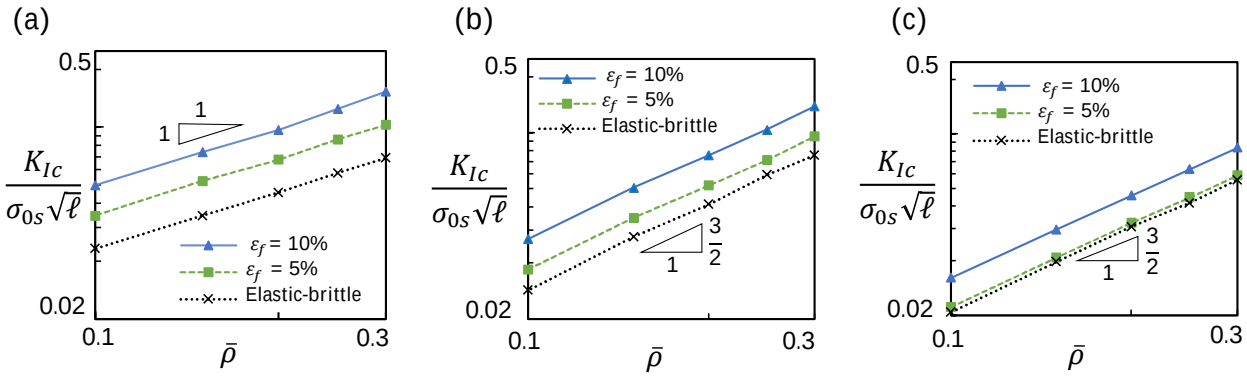

Figure 5: Normalised fracture toughness as a function of relative density for (a) snub-trihexagonal, (b) snub-square, and (c) elongated-triangular lattices. Results are shown for a strain hardening exponent $n = 13$ and different values of failure strain ϵ_f.

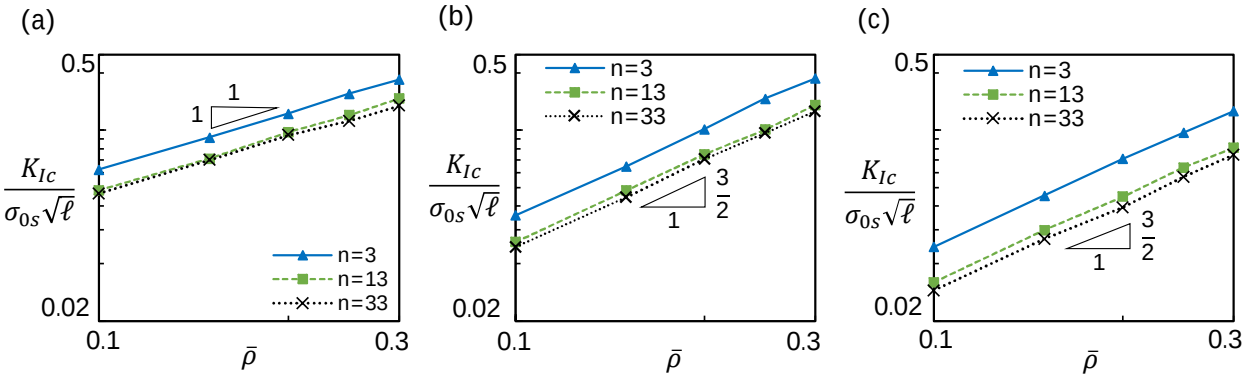

Figure 6: Normalised fracture toughness as a function of relative density for (a) snub-trihexagonal, (b) snub-square, and (c) elongated-triangular lattices. Results are shown for a failure strain $\epsilon_f = 0.1$ and different values of strain hardening exponent n.

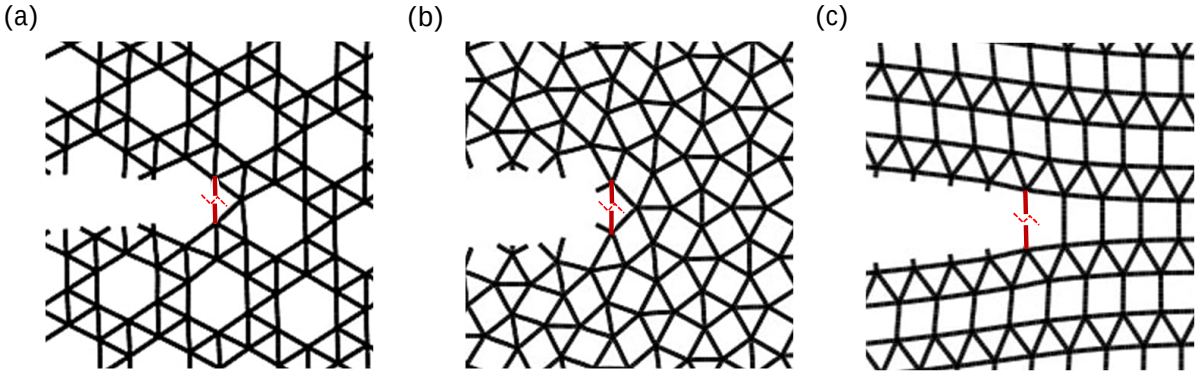

Figure 7: Deformed meshes at the moment of initial fracture for (a) snub-trihexagonal, (b) snub-square, and (c) elongated-triangular lattices. Results are shown for $\bar{\rho} = 0.25$, $\epsilon_f = 0.1$, and $n = 13$. The first cell wall to fracture is indicated in red.

Table 2: Parameters D, D', and d for the scaling laws in Eq. (1) and (3). Results for D' are given for different values of strain hardening exponent n, whereas D corresponds to an elastic-brittle material.

Topology	D	D'				d
		$n = 3$	$n = 13$	$n = 23$	$n = 33$	
Snub-trihexagonal	0.46	0.45	0.44	0.42	0.42	1
Snub-square	0.95	0.83	0.75	0.73	0.73	1.5
Elongated-triangular	0.71	0.58	0.45	0.42	0.42	1.5

Clearly, increasing the failure strain ϵ_f increases the fracture toughness of all three lattices, see Fig. 5. For example, the fracture toughness of a snub-trihexagonal lattice increases by 127% when an elastic-brittle parent material is replaced by a ductile solid with $\epsilon_f = 0.1$ and $n = 13$. This increase is sensitive to architecture; being 87% for the snub-square and 50% for the elongated-triangular lattice. On the other hand, increasing n decreases the fracture toughness, see Fig. 6. This reduction, however, saturates around $n = 33$ as the response of the parent material becomes elastic perfectly-plastic, see Eq. (2).

The results in Fig. 5 and 6 were used to find the parameters D, D' and d for the scaling laws introduced earlier in Eq. (1) and (3). The results, summarised in Table 2, show that D' varies significantly with n for both the snub-square and elongated-triangular lattices. This is, however, not the case for the stretching-dominated snub-trihexagonal lattice. These observations are in-line with the results of Tankasala et al. (2015); their simulations showed that D' is sensitive to n for the diamond and hexagonal lattices, whereas D' is roughly constant for the stretching-dominated triangular lattice.

Next, we turn our attention to the exponent d of the scaling law, see Eq. (1) and (3). The fracture toughness of a snub-trihexagonal lattice scales linearly with relative density, which gives $d = 1$, see Fig. 5a and 6a. In contrast, $d = 1.5$ for snub-square and elongated-triangular lattices. Results in Fig. 5 and 6 show that this scaling is insensitive to the failure strain ϵ_f and the degree of strain hardening n.

3.2. Experimental results

Force versus displacement curves are plotted in Fig. 8 for the three semi-regular lattices with a relative density $\bar{\rho} = 0.25$. In all cases, the response is linear up to the peak force P_{max}, which corresponds to the first fracture event. Photographs showing the deformation of the

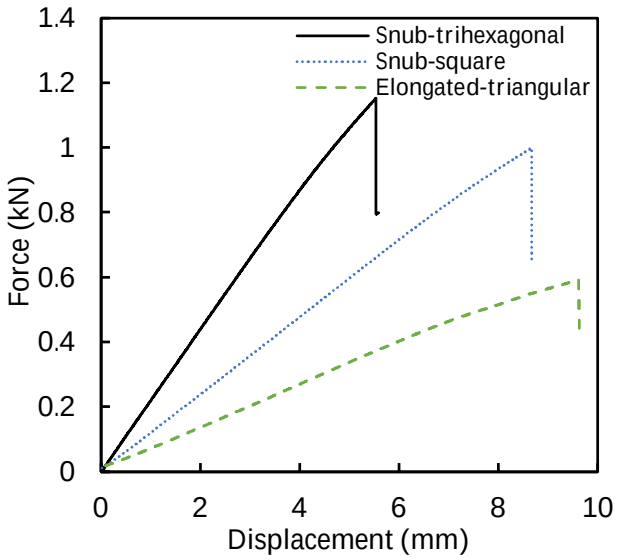

Figure 8: Force versus load-line displacement recorded during fracture toughness tests. Responses are shown for a relative density $\bar{\rho} = 0.25$.

samples before and after fracture are given in Fig. 9. Multiple bars fail in the first fracture event, starting with the vertical cell wall ahead of the crack tip, as predicted numerically (see Fig. 7). The tests on samples with $\bar{\rho} = 0.2$ and 0.3 are not shown here, but they had a similar crack propagation path and also had a linear response, which justifies the use of Eq. (5) to calculate the fracture toughness.

The normalised fracture toughness is plotted in Fig. 10 as a function of relative density for the three architectures considered in this study. Two samples were tested for each geometry and both data points are included in Fig. 10. In general, the scatter is small; the average difference between tests is 4%, and the largest difference is 11%. This can be attributed to the variability of the failure strain of the polymer, which is $\epsilon_f = 0.10 \pm 0.02$ as mentioned in Section 2.2.

The measurements are also compared to FE simulations in Fig. 10. These numerical results are reproduced from Fig. 5 and correspond to the case where $\sigma_{0s} = 45\,\text{MPa}$, $\epsilon_{0s} = 0.02$, $\epsilon_f = 0.1$, and $n = 13$. These material properties were obtained by fitting the measured tensile response of the polymer, and we can see in Fig. 4 that this Ramberg-Osgood description follows closely the measured stress-strain curve. The scaling law in Eq. (3), which is fitted

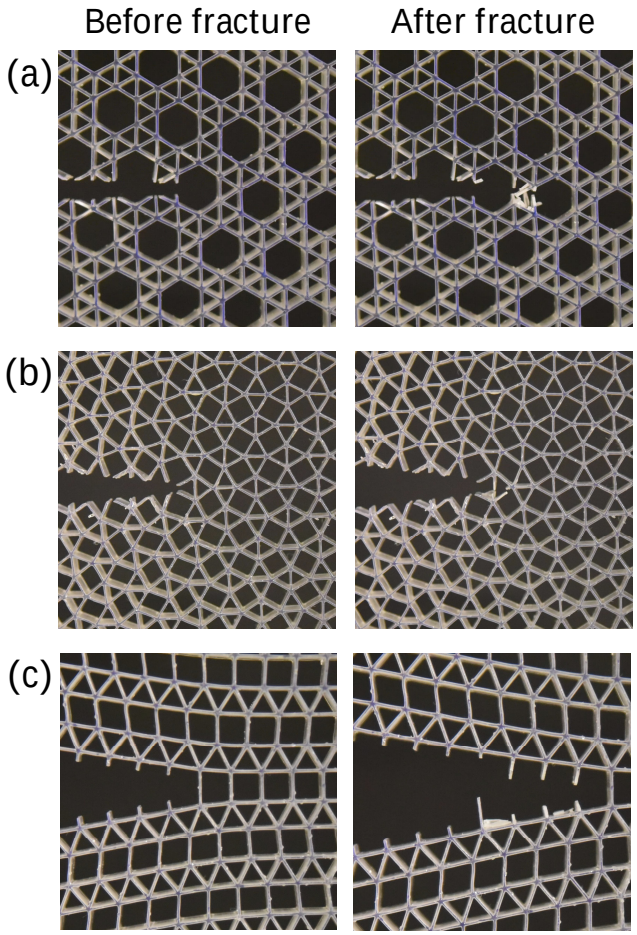

Figure 9: Photographs of the fracture toughness tests for (a) snub-trihexagonal, (b) snub-square, and (c) elongated-triangular lattices with a relative density $\bar{\rho} = 0.25$. Photographs are shown right before and after the first fracture event. For scale, all bars have a length of 6 mm.

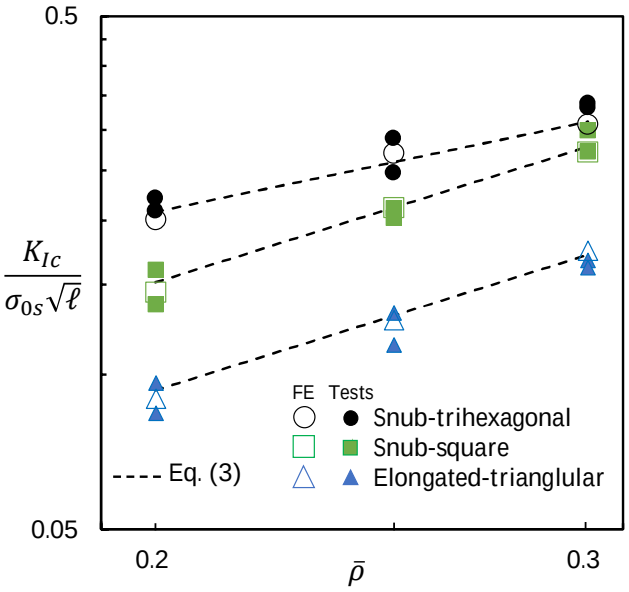

Figure 10: Comparison between fracture toughness tests and FE predictions. The material properties used in the simulations are $\sigma_{0s} = 45\,\text{MPa}$, $\epsilon_{0s} = 0.02$, $\epsilon_f = 0.1$, and $n = 13$. The scaling law, Eq.(3), is included for completeness.

on these numerical results, is also included in Fig. 10 for completeness. There is an excellent agreement between measurements and FE predictions, and this holds true for the three semi-regular lattices considered. This agreement is remarkable considering that the specimens tested had about 10 times fewer unit cells than the FE simulations (compare the dimensions in Fig. 1a and 3). These results suggest that the asymptotic fracture toughness can be measured with CT samples where the width W and the length ℓ of the cell walls are such that $W/\ell \approx 30$ or higher. Interestingly, the numerical simulations done by Gu et al. (2019) suggested a similar size requirement for the 3D octet truss.

4. Discussion

In this section, we compare the fracture toughness of the three semi-regular lattices to that of regular tessellations. This is done by contrasting parameters D and d in Table 2 with the data given in Table 1. First, we can see that the snub-trihexagonal lattice has very similar performances to the triangular tessellation; they both have $d = 1$, but the value of D is 8% lower for the snub-trihexagonal lattice. Second, the results show that the snub-square

and elongated-triangular lattices have a unique behaviour since they are the only prismatic lattices with $d = 1.5$. The mechanisms leading to $d = 1.5$ can be described with an analytical model, which is detailed below. This analysis is based on the work done by Tankasala et al. (2015) for isotropic topologies and it is extended here for orthotropic lattices.

Consider a snub-square or elongated-triangular lattice with a semi-infinite crack loaded in mode I as shown in Fig. 2. In the vicinity of the crack tip, the the J-integral is related to the macroscopic stress σ_{22} and strain ϵ_{22} by:

$$J \propto \sigma_{22}\, \epsilon_{22}\, x_1. \tag{6}$$

Both the snub-square and elongated-triangular lattices are stretching-dominated when loaded in the x_2 direction (Omidi and St-Pierre, 2022). Therefore, the axial tensile stress σ_b and strain ϵ_b in a bar close to the crack tip are related to the macroscopic stress and strain as:

$$\sigma_{22} \propto \bar{\rho}\sigma_b \qquad \text{and} \qquad \epsilon_{22} \propto \epsilon_b. \tag{7}$$

Substituting these expressions in Eq. (6) yields:

$$J \propto \bar{\rho}\sigma_b\epsilon_b\, x_1. \tag{8}$$

Next, we can estimate the toughness J_c by setting $\epsilon_b = \epsilon_f$ at a distance $x_1 = \ell$. Neglecting the linear term in Eq. (2), the corresponding stress $\sigma_b \approx \sigma_{0s}(\epsilon_f/\epsilon_{0s})^{1/n}$ and the above expression becomes:

$$J_c \propto \left(\frac{\epsilon_f}{\epsilon_{0s}}\right)^{\frac{n+1}{n}} \sigma_{0s}\, \epsilon_{0s}\, \bar{\rho}\, \ell. \tag{9}$$

The relationship between the J-integral and the stress intensity factor K_I for orthotropic materials is detailed in (Suo et al., 1991). The expression depends on the degree of anisotropy, but we show in Appendix B that for the snub-square and elongated-triangular lattices it can be approximated as:

$$J \approx \frac{K_I^2}{2E_2}\sqrt{\frac{E_2}{G_{12}}}, \tag{10}$$

where E_2 is the elastic modulus in x_2 and G_{12} is the in-plane shear modulus of the lattice. For both snub-square and elongated-triangular lattices, $E_2 \propto \bar{\rho} E_s$ and $G_{12} \propto \bar{\rho}^3 E_s$ (Omidi and St-Pierre, 2022). Substituting these expressions and Eq. (9) in (10) yields:

$$K_{Ic} \propto \bar{\rho}^{1.5} \sigma_{0s} \sqrt{\ell} \left(\frac{\epsilon_f}{\epsilon_{0s}} \right)^{\frac{n+1}{2n}}, \tag{11}$$

which is in the form of Eq. (3) and includes the correct exponent $d = 1.5$. To summarise, the above analysis shows that the constant $d = 1.5$ is due to two contributing factors. First, the zone of tensile deformation close to the crack tip, which is visible in Fig. 7 and reflected in Eq. (7). Second, the orthotropic behaviour of both snub-square and elongated-triangular lattices, which leads to Eq. (10). It is relevant to mention here that the mode I fracture toughness of elastic-brittle foams and the mode II fracture toughness of a square 0/90° lattice also scale as $\bar{\rho}^{1.5}$ (Maiti et al., 1984; Romijn and Fleck, 2007). We emphasise, however, that the mechanisms are different from those observed in this study. In foams and for the square lattice in shear, the cell walls are failing in bending, whereas tensile fracture dominates for the two semi-regular lattices considered in this study.

Finally, our numerical and experimental results show that the snub-square is tougher than the elongated-square lattice, see Fig. 10, and this can also be explained with the above analytical expressions. Omidi and St-Pierre (2022) showed that the snub-square lattice has a much higher shear modulus G_{12} than the elongated-square, even though both lattices have a similar elastic modulus E_2. We can see from Eq. (10) how a higher shear modulus G_{12} will lead to a higher fracture toughness K_{Ic}.

5. Conclusion

The fracture toughness of three ductile semi-regular lattices was investigated using FE simulations and experiments. We found that the snub-trihexagonal lattice has a fracture toughness that scales linearly with relative density $\bar{\rho}$ and is very similar to that of a triangular lattice. In contrast, the fracture toughness of snub-square and elongated-triangular lattices scales as $\bar{\rho}^{1.5}$, where the exponent of 1.5 is unique amongst prismatic lattices loaded in mode I. We showed analytically that this is a consequence of the tensile deformation at the crack

tip and the orthotropic behaviour of these two tessellations. For the three architectures considered, the fracture toughness predicted by FE simulations was in excellent agreement with experiments performed on CT samples produced by additive manufacturing. This demonstrates that it is possible to accurately measure the fracture toughness of ductile lattice materials even though experiments are done with significantly fewer unit cells that what is typically used in FE simulations. Our results will be beneficial for the design of specimens in future experimental studies, and the development of guidelines to measure the fracture toughness of lattice materials.

This study was limited to the onset of fracture and did not cover the resistance to crack growth (R-curve). Recent work by Tankasala and Fleck (2020) and Hsieh et al. (2020) has shown that some architectures, such as the triangular lattice, have a rising R-curve and future work is needed to determine if the three semi-regular lattices considered in this study also exhibit a strong resistance to crack propagation.

Acknowledgements

This work was supported by the Academy of Finland [decision 322007].

References

Alsalla, H., Hao, L., Smith, C., 2016. Fracture toughness and tensile strength of 316L stainless steel cellular lattice structures manufactured using the selective laser melting technique. Mater. Sci. Eng. A 669, 1–6. doi:10.1016/j.msea.2016.05.075.

Ashby, M.F., 1983. Mechanical properties of cellular solids. Metall. Trans. A 14, 1755–1769. doi:10.1007/BF02645546.

ASTM E1820, 2018. Standard test method for measurement of fracture toughness. ASTM Book of Standards. doi:10.1520/E1820-18.

Berger, J.B., Wadley, H.N.G., McMeeking, R.M., 2017. Mechanical metamaterials at the theoretical limit of isotropic elastic stiffness. Nature 543, 533–537. doi:10.1038/nature21075.

Berkache, K., Phani, S., Ganghoffer, J.F., 2022. Micropolar effects on the effective elastic properties and elastic fracture toughness of planar lattices. Eur. J. Mech. A Solids 93, 104489. doi:10.1016/j.euromechsol.2021.104489.

Chen, J.Y., Huang, Y., Ortiz, M., 1998. Fracture analysis of cellular materials: a strain gradient model. J. Mech. Phys. Solids 46, 789–828. doi:10.1016/S0022-5096(98)00006-4.

Daynes, S., Lifton, J., Lu, W.F., Wei, J., Feih, S., 2021. Fracture toughness characteristics of additively manufactured Ti–6Al–4V lattices. Eur. J. Mech. A Solids 86, 104170. doi:10.1016/j.euromechsol.2020.104170.

Fleck, N.A., Qiu, X.M., 2007. The damage tolerance of elastic-brittle, two-dimensional isotropic lattices. J. Mech. Phys. Solids 55, 562–588. doi:10.1016/j.jmps.2006.08.004.

Gibson, L.J., Ashby, M.F., 1997. Cellular Solids. Cambridge University Press. doi:10.1017/CBO9781139878326.

Gu, H., Li, S., Pavier, M., Attallah, M.M., Paraskevoulakos, C., Shterenlikht, A., 2019. Fracture of three-dimensional lattices manufactured by selective laser melting. Int. J. Solids Struct. 180-181, 147–159. URL: https://doi.org/10.1016/j.ijsolstr.2019.07.020, doi:10.1016/j.ijsolstr.2019.07.020.

Gu, H., Pavier, M., Shterenlikht, A., 2018. Experimental study of modulus, strength and toughness of 2D triangular lattices. Int. J. Solids Struct. 152-153, 207–216. doi:10.1016/j.ijsolstr.2018.06.028.

Hsieh, M.T., Deshpande, V.S., Valdevit, L., 2020. A versatile numerical approach for calculating the fracture toughness and R-curves of cellular materials. J. Mech. Phys. Solids 138, 103925. doi:10.1016/J.JMPS.2020.103925.

Hsieh, M.T., Endo, B., Zhang, Y., Bauer, J., Valdevit, L., 2019. The mechanical response of cellular materials with spinodal topologies. J. Mech. Phys. Solids 125, 401–419. doi:10.1016/J.JMPS.2019.01.002.

Huang, J.S., Gibson, L.J., 1991. Fracture toughness of brittle honeycombs. Acta Metall. Mater. 39, 1617–1626. doi:10.1016/0956-7151(91)90249-Z.

Li, T., Jarrar, F., Abu Al-Rub, R., Cantwell, W., 2021. Additive manufactured semi-plate lattice materials with high stiffness, strength and toughness. Int. J. Solids Struct. 230-231, 111153. doi:10.1016/j.ijsolstr.2021.111153.

Lipperman, F., Ryvkin, M., Fuchs, M.B., 2007. Fracture toughness of two-dimensional cellular material with periodic microstructure. Int. J. Fract. 146, 279–290. doi:10.1007/s10704-007-9171-5.

Liu, C., Rosakis, A.J., Ellis, R.W., Stout, M.G., 1998. A study of the fracture behavior of unidirectional fiber-reinforced composites using Coherent Gradient Sensing (CGS) interferometry. Int. J. Fract. 90, 355–382. doi:10.1023/A:1007479709559.

Liu, Y., St-Pierre, L., Fleck, N.A., Deshpande, V.S., Srivastava, A., 2020. High fracture toughness micro-architectured materials. J. Mech. Phys. Solids 143, 104060. doi:10.1016/J.JMPS.2020.104060.

Maiti, S.K., Ashby, M.F., Gibson, L.J., 1984. Fracture toughness of brittle cellular solids. Scr. Mater. 18, 213–217. doi:10.1016/0036-9748(84)90510-6.

O'Masta, M.R., Dong, L., St-Pierre, L., Wadley, H.N., Deshpande, V.S., 2017. The fracture toughness of octet-truss lattices. J. Mech. Phys. Solids 98, 271–289. doi:10.1016/j.jmps.2016.09.009.

Omidi, M., St-Pierre, L., 2022. Mechanical properties of semi-regular lattices. Mater. Des. 213, 110324. doi:10.1016/j.matdes.2021.110324.

Quintana-Alonso, I., Fleck, N.A., 2007. Damage tolerance of an elastic-brittle diamond-celled honeycomb. Scr. Mater. 56, 693–696. doi:10.1016/j.scriptamat.2006.12.027.

Quintana-Alonso, I., Fleck, N.A., 2009. Fracture of brittle lattice materials: a review, in: Daniel, I.M., Gdoutos, E.E., Rajapakse, Y.D.S. (Eds.), Major accomplishments in composite materials and sandwich structures, Springer Netherlands, Dordrecht. pp. 799–816. doi:10.1007/978-90-481-3141-9_30.

Quintana-Alonso, I., Mai, S.P., Fleck, N.A., Oakes, D.C., Twigg, M.V., 2010. The fracture toughness of a cordierite square lattice. Acta Mater. 58, 201–207. doi:10.1016/J.ACTAMAT.2009.08.069.

Romijn, N.E., Fleck, N.A., 2007. The fracture toughness of planar lattices: imperfection sensitivity. J. Mech. Phys. Solids 55, 2538–2564. doi:10.1016/j.jmps.2007.04.010.

Schmidt, I., Fleck, N.A., 2001. Ductile fracture of two-dimensional cellular structures. Int. J. Fract. 111, 327–342. doi:10.1023/A:1012248030212.

Seiler, P.E., Tankasala, H.C., Fleck, N.A., 2019. The role of defects in dictating the strength of brittle honeycombs made by rapid prototyping. Acta Mater. 171, 190–200. doi:10.1016/j.actamat.2019.03.036.

Shaikeea, A.J.D., Cui, H., O'Masta, M., Zheng, X.R., Deshpande, V.S., 2022. The toughness of mechanical metamaterials. Nat. Mater. 21, 297—304. doi:10.1038/s41563-021-01182-1.

Suo, Z., 1990. Delamination specimens for orthotropic materials. J. Appl. Mech. 57, 627–634. doi:10.1115/1.2897068.

Suo, Z., Bao, G., Fan, B., Wang, T.C., 1991. Orthotropy rescaling and implications for fracture in composites. Int. J. Solids Struct. 28, 235–248. doi:10.1016/0020-7683(91)90208-W.

Tancogne-Dejean, T., Diamantopoulou, M., Gorji, M.B., Bonatti, C., Mohr, D., 2018. Metamaterials: 3D

plate-lattices: an emerging class of low-density metamaterial exhibiting optimal isotropic stiffness. Adv. Mater. 30, 1870337. doi:10.1002/ADMA.201870337.
Tankasala, H.C., Deshpande, V.S., Fleck, N.A., 2015. 2013 Koiter medal paper: Crack-tip fields and toughness of two-dimensional elastoplastic lattices. J. Appl. Mech. 82, 1–10. doi:10.1115/1.4030666.
Tankasala, H.C., Fleck, N.A., 2020. The crack growth resistance of an elastoplastic lattice. Int. J. Solids Struct. 188-189, 233–243. doi:10.1016/J.IJSOLSTR.2019.10.007.
Williams, M.L., 1952. On the stress distribution at the base of a stationary crack. J. Appl. Mech. 19, 109–114. doi:10.1115/1.4011454.
Williams, R., 1979. The geometrical foundation of natural structure: a source book of design. Dover, New York.

Appendix A. Influence of the number of unit cells on the apparent fracture toughness

Additional FE simulations were conducted to ensure that the CT samples used in experiments had a sufficiently large number of cells to provide an accurate measurement of the fracture toughness. In these simulations, the overall dimensions of the CT samples were kept fixed (W, H, B and a in Fig. 3), but the number of cells was varied by changing the bar length ℓ. The geometry was meshed using beam elements (B21 in Abaqus notation) with 20 elements per bar. The material properties were representative of the polymer used in experiments and tabulated from the tensile test in Fig. 4.

The normalised fracture toughness is plotted in Fig. A.1 as a function of the normalised number of cells W/ℓ (where W is the width of the CT sample and ℓ is the length of a cell wall). For all lattices, the normalised fracture toughness decreases with increasing number of cells, until it reaches an asymptotic value around $W/\ell \approx 30$. The dimensions used in experiments ($\ell = 6\,\text{mm}$) are indicated in Fig. A.1; in all cases, the number of cells is sufficiently large to measure the asymptotic fracture toughness. The data in Fig. A.1 is limited to a relative density $\bar{\rho} = 0.3$, but lower relative densities showed the same trend.

Appendix B. Relationship between J and K_I for orthotropic lattices

The snub-square and elongated-triangular lattices both have an orthotropic in-plane elastic response. Assuming a state of plane stress and using the reference frame in Fig. 2,

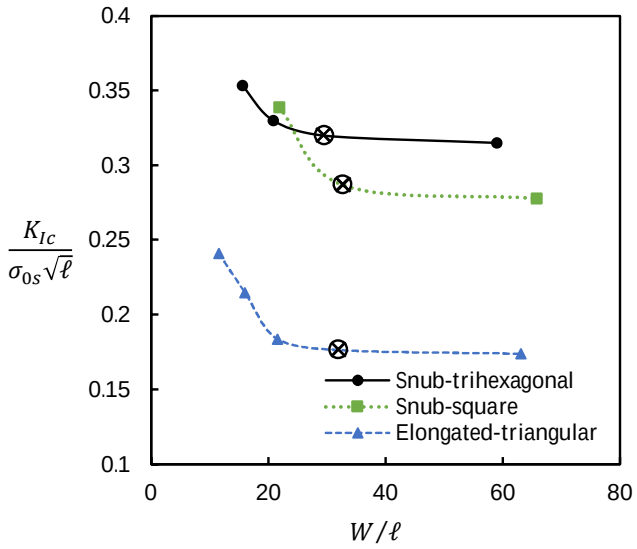

Figure A.1: Normalised fracture toughness as a function of the normalised number of cells in a CT sample. The dimensions used in experiments are shown with ⊗. Results are shown for a relative density $\bar{\rho} = 0.3$.

the macroscopic stresses and strains are related by (Quintana-Alonso et al., 2010):

$$\begin{bmatrix} \epsilon_{11} \\ \epsilon_{22} \\ \epsilon_{12} \end{bmatrix} = \begin{bmatrix} A_{11} & A_{12} & 0 \\ A_{12} & A_{22} & 0 \\ 0 & 0 & A_{33} \end{bmatrix} \begin{bmatrix} \sigma_{11} \\ \sigma_{22} \\ \sigma_{12} \end{bmatrix}, \tag{B.1}$$

where the terms of the compliance matrix are related to the conventional elastic properties as:

$$\begin{aligned} A_{11} &= 1/E_1 \\ A_{22} &= 1/E_2 \\ A_{12} &= -\nu_{21}/E_2 = -\nu_{12}/E_1 \\ A_{22} &= 1/G_{12}. \end{aligned} \tag{B.2}$$

These elastic properties were derived analytically by Omidi and St-Pierre (2022) and their results are summarised in Table B.1 for both snub-square and elongated-triangular lattices.

For a linear elastic orthotropic solid, the J-integral is related to the mode I stress intensity factor by (Suo, 1990; Suo et al., 1991):

$$J = \sqrt{\frac{1+\rho}{2}} \lambda^{1/4} A_{22} K_I^2, \tag{B.3}$$

Table B.1: Elastic properties for both snub-square and elongated-triangular lattices. The moduli are expressed as a function of the relative density $\bar{\rho}$ and of the elastic modulus E_s of the parent material (Omidi and St-Pierre, 2022).

Topology	$E_1 = E_2$	G_{12}	$\nu_{12} = \nu_{21}$
Snub-square	$0.280\bar{\rho}E_s$	$0.443\bar{\rho}^3E_s$	0.433
Elongated-triangular	$0.408\bar{\rho}E_s$	$0.078\bar{\rho}^3E_s$	0.158

where

$$\lambda = \frac{A_{11}}{A_{22}} \qquad \text{and} \qquad \rho = \frac{2A_{12} + A_{33}}{2\sqrt{A_{11}A_{22}}}. \tag{B.4}$$

With the relations in Eq. (B.2) and the properties in Table B.1, we find that:

$$\lambda = 1 \qquad \text{and} \qquad \rho = \frac{E_2}{2G_{12}} - 2\nu_{12} \approx \frac{E_2}{2G_{12}}, \tag{B.5}$$

where the above simplification is based on the fact that $G_{12} \ll E_2$ for low values of $\bar{\rho}$, see Table B.1. Finally, substituting Eq. (B.5) and $\lambda = 1$ in (B.3) returns:

$$J = \sqrt{\frac{2G_{12} + E_2}{4G_{12}}}\frac{K_I^2}{E_2} \approx \frac{K_I^2}{2E_2}\sqrt{\frac{E_2}{G_{12}}}, \tag{B.6}$$

which is the relationship used in Eq. (10).